Received: 25 November 2022 | Revised: 25 January 2023 | Accepted: 14 February 2023

DOI: 10.1111/jace.19076

Journal of the American Ceramic Society

RESEARCH ARTICLE

# Prediction of ring crack initiation in ceramics and glasses using a stress–energy fracture criterion

**Roman Papšík**[1] | **Oldřich Ševeček**[2] | **Éric Martin**[3] | **Raúl Bermejo**[1]

[1]Department of Materials Science, Montanuniversität Leoben, Leoben, Austria

[2]Institute of Solid Mechanics, Mechatronics and Biomechanics, Faculty of Mechanical Engineering, Brno University of Technology, Brno, Czech Republic

[3]Laboratory of Thermo Structural Composites, Bordeaux INP, Université de Bordeaux, CNRS UMR, Pessac, France

**Correspondence**
Raúl Bermejo, Department of Materials Science, Montanuniversität Leoben, Franz Josef-Straße 18, 8700 Leoben, Austria.
Email: raul.bermejo@unileoben.ac.at

**Editor's Choice**
The Editor-in-Chief recommends this outstanding article.

**Funding information**
European Research Council, Grant/Award Number: program Horizon 2020

**Abstract**

Crack initiation in brittle materials upon spherical indentation is associated with the tensile radial stresses during loading. However, location of crack onset often differs (offset) from the site of maximal stress. In addition, experiments reveal a strong dependency of crack initiation forces on geometrical parameters as well as the surface condition of the sample. In this work, a coupled stress–energy fracture criterion is introduced to describe the initiation of ring cracks in brittle materials, which takes into account the geometry of the contact and the inherent strength and fracture toughness of the material. Several experiments reported in literature are evaluated and compared. The criterion can explain the location offset of the ring crack upon loading, as observed in various ceramics and glasses. It also predicts the ring crack initiation force upon contact loading, provided that surface compressive stresses, introduced during grinding or polishing processes, are taken into account. Furthermore, the stress–energy criterion may be employed to estimate the surface residual stress of ceramic parts, based on simple contact damage experiments.

**KEYWORDS**
brittle fracture, coupled criterion, crack initiation, finite fracture mechanics, ring crack

## 1 | INTRODUCTION

Fracture of brittle materials caused by contact with a hard spherical indenter has been studied since the end of 19th century motivated by the characterization of material hardness.[1] When a hard spherical indenter (a ball) is pushed onto a flat surface of a brittle material (glass or ceramic), a crack with the shape of a ring usually develops, which can further extend into a cone crack as depicted schematically in Figure 1A. Experimental evidence of a ring crack extended into a cone crack on an alumina ceramic is shown in Figure 1B. The initial ring crack is typically perpendicular to the surface.

Ball indentation induces not only compressive stresses under the contact zone, but also tensile radial stresses in the vicinity of the indenter. Induced stresses can be calculated using the Hertz contact theory,[3] which is an analytical model of the contact between two geometrically smooth bodies with linear elastic material response and no friction between them. The contact radius $R_c$ depends on the applied force $F$, the ball radius $R_b$, and the contact stiffness $E_c$, according to the following relation:

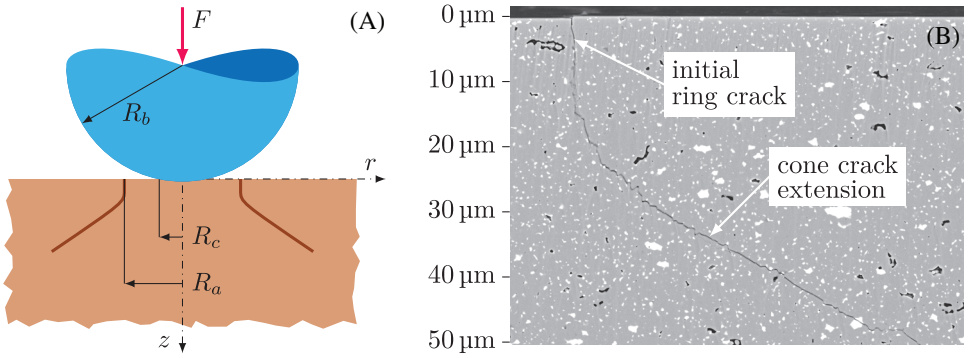


**FIGURE 1** (A) Schematic depiction of indentation of a sphere into a brittle material. $F$ is the applied force, $R_b$ is the ball radius, $R_c$ is the contact radius, and $R_a$ is the crack radius. (B) Cross section of a Hertzian crack.[2]

$$R_c = \sqrt[3]{\frac{3FR_b}{4E_c}} \tag{1}$$

with $E_c$ given by

$$E_c = \left(\frac{1-\nu_b^2}{E_b} + \frac{1-\nu_s^2}{E_s}\right)^{-1} \tag{2}$$

where $E_b$, $E_s$, $\nu_b$, and $\nu_s$ are Young's moduli and Poisson's ratios of the ball and specimen, respectively.

Upon crack initiation, the maximum radial stress, $\sigma_{r,\max}$, which coincides with the maximum first-principal stress, $\sigma_{I,\max}$, is located on the surface at the contact radius.[4] Using a simple maximum stress criterion for fracture, when $F = F_c$ the following relationship is obtained:

$$\sigma_{r,\max} = \sigma_{I,\max} = \frac{1-2\nu_s}{\pi}\sqrt[3]{\frac{2E_c^2F_c}{9R_b^2}} = \sigma_c, \tag{3}$$

where $F_c$ is the crack initiation force and $\sigma_c$ is the material tensile strength.

## 1.1 | Crack initiation force dependency on the ball radius

In one of the earliest experiments with glass, Auerbach[1] observed that the fracture force depended linearly on the ball radius, which is today commonly known as the Auerbach law. Using larger balls, Tillet[5] observed that the linear dependency holds only up to a specific size of the indenter, after which a kink occurs. As the ball radius increases, the dependency becomes asymptotically quadratic. The same behavior was confirmed by other experiments.[6] Besides glasses, vitreous carbon also exhibited the Auerbach law.[7]

Figure 2 depicts the dependency of the crack initiation forces on ball radii from experiments with different glass surface conditions. The influence of surface etching was examined by Hamilton and Rawson.[8] They observed that etching strengthens the material and increases the crack initiation forces. Mouginot and Maugis[9] conducted experiments with glass having various surface machining and observed that abrasion by an SiC paper produces the Auerbach law but polishing by a diamond paste followed the dependency $F_c/R_b^{1.3} =$ constant.

One of the first indentation experiments on a ceramic material was performed by Miller and Bowman,[10] who investigated the fracture of textured $Si_3N_4$. Wereszczak et al.[11] investigated the fracture of SiC indented by diamond balls using an acoustic emission method. More recently, the method has been extended and applied by Schlacher et al.[2] to $Al_2O_3$ with equiaxial and textured microstructures indented by WC balls.

The dependence of crack initiation force on ball radii from selected experiments with ceramics is plotted in Figure 3. On the one hand, SiC indented by diamond or SiC balls and $Al_2O_3$ indented by WC balls exhibit the Auerbach law. On the other hand, $Si_3N_4$ indented by WC balls exhibits the $F_c/R_b^{1.7} =$ constant dependency. Although there is not enough data to claim a clear ball radius dependency for the experiments with $Si_3N_4$ indented by $Si_3N_4$ balls, there is evidence that annealing seems to affect (decrease) the crack initiation force.

## 1.2 | Location of ring crack formation

Another typical feature of indentation experiments is the radius of the ring crack. It has been observed that crack radii are larger than the contact radii by ~12% for silicate glass indented by steel balls,[5] 20%–23% for silicate glass indented by beryllia balls,[14] ~17% for vitreous carbon indented by steel balls,[7] 10%–20% for silicon carbide

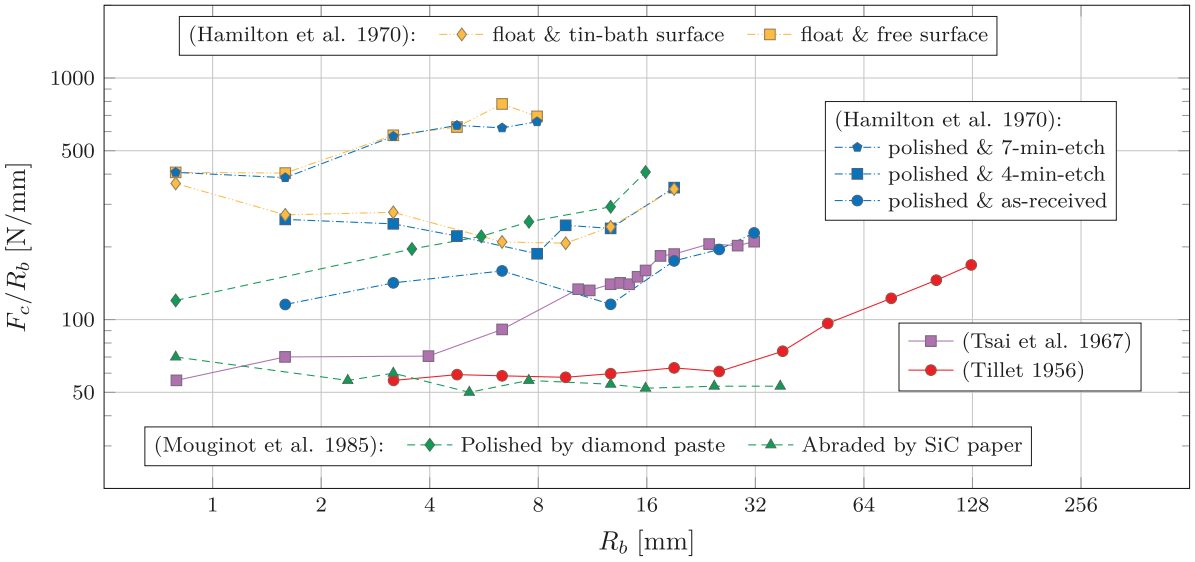


**FIGURE 2** Fracture forces $F_c$ normalized by ball radii $R_b$ for indentation of glasses by steel balls.[5,6,8,9]

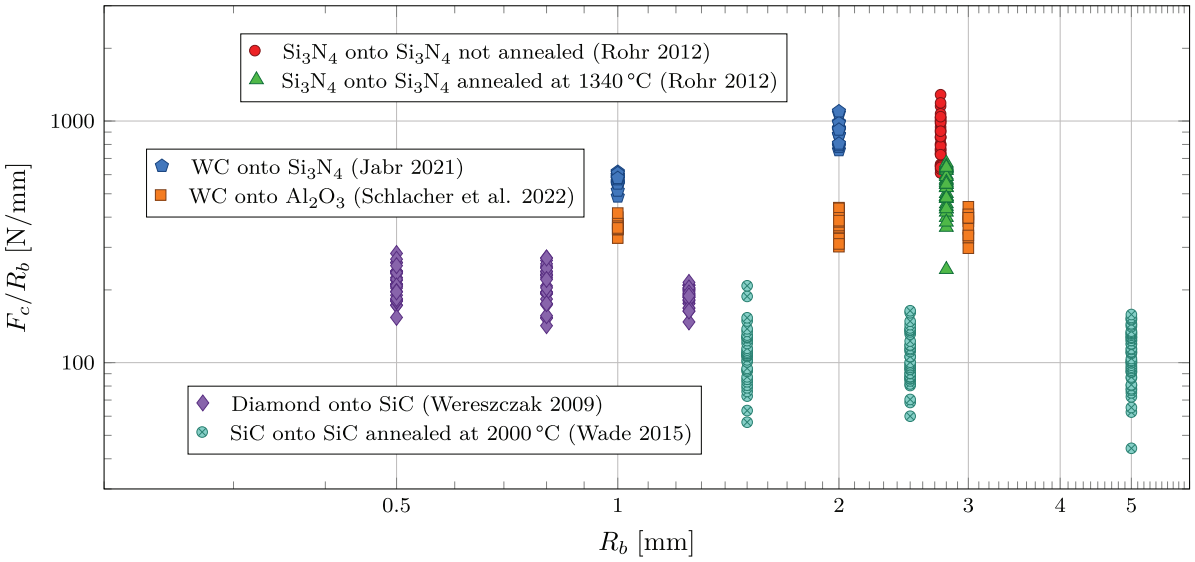


**FIGURE 3** Crack initiation forces $F_c$ normalized by ball radii $R_b$ for indentation of ceramics by various balls.[11,12,13,2]

indented by diamond balls,[11] and 10%–26% for soda–lime–silica glass indented by tungsten carbide balls,[15] among others. Recent work from Schlacher et al.[2] showed that for $Al_2O_3$ and $Si_3N_4$ indented by WC balls cracks may be 20%–40% larger than the contact radius (Figure 4), which seems inconsistent with other reported values. In the case of $Si_3N_4$ indented by WC balls, additional experiments were done to analyze the effect of friction due to contact. Although this changes the magnitude of stresses and the location of their maximum, there was no significant change in the crack initiation force or the crack size between the dry and lubricated (with oil applied) contact. Preliminary finite element simulations with various coefficients of friction did not show any significant effect on the crack initiation forces either.

## 1.3 | Influence of surface residual stresses

An important issue is associated with the residual stress state on the surface of the material prior to indentation. A systematic study was performed by Rohr,[12] who indented $Si_3N_4$ with a single size ball of the same material to

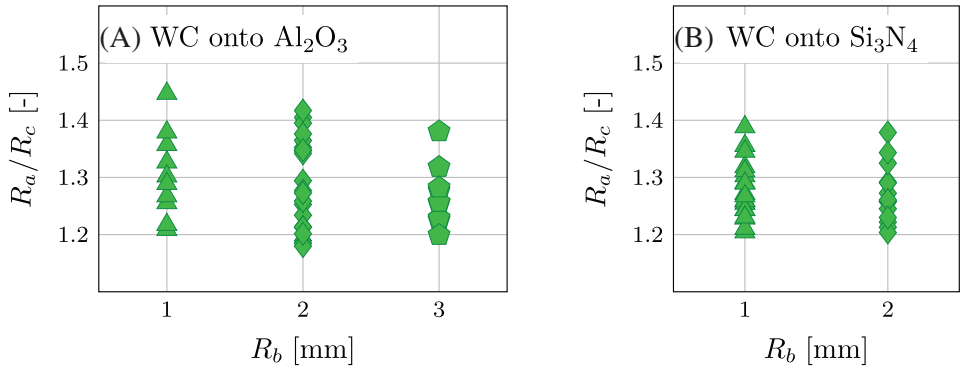


**FIGURE 4** Crack radii $R_a$ normalized by theoretical contact radii $R_c$ produced by indentation of (A) $Al_2O_3$[2] and (B) $Si_3N_4$ specimen[16] by WC balls with different radii $R_b$.

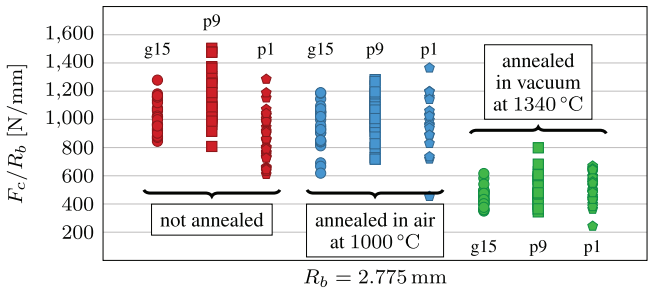


**FIGURE 5** Effect of annealing and surface polishing (g15: ground to 15 $\mu$m, p9: polished to 9 $\mu$m, p1: polished to 1 $\mu$m) on the fracture forces.[12]

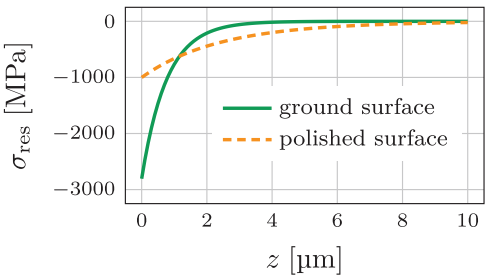


**FIGURE 6** X-ray diffraction (XRD) measurement of biaxial residual stress $\sigma_{res}$ plotted over the depth $z$ in specimens with different surface machining. *Source*: Adopted from Ref. [17] by averaging measurements in two directions.

examine the influence of different surface qualities on the crack initiation force (Figure 5).

The effect of annealing was also studied in that investigation. Interestingly, annealing in air at 1000°C for 5 h did not change the crack initiation force significantly, but annealing in vacuum at 1340°C for 4 h decreased the crack initiating force by ~45%. This could be explained by the relaxation of residual stress at the surface, as demonstrated through experimental measurements in $Si_3N_4$ (Figure 6), using equipenetration grazing incidence X-ray diffraction (XRD).[17] Additionally, a specimen was ground by a diamond grinding wheel of grit D15, and another specimen was further polished by diamond suspensions with 1 $\mu$m mean particle size. They concluded that the compressive residual stresses were almost biaxial and could reach up to −3 and −1 GPa on top of the ground and polished surface, respectively. However, the stresses vanished very rapidly below the surface; they decreased by approximately 90% within 2 and 6 $\mu$m of depth below the ground and the polished surface, respectively.

## 1.4 | Approaches to explaining crack initiation

There are two main approaches aiming to explain the Auerbach law and the ring crack location: (i) the flaw statistics approach and (ii) the energy balance approach. Many arguments exist for and against both approaches, based on experimental evidence or computational models, as reviewed in Ref. [18]. Effect of friction, nonlinear deformations, flaw distributions, and crack growth have also received attention.

When empirically observed ratio $F_c/R_b$ = constant holds and if the maximum stress criterion is used, according to Equation (3), the material strength would be a function of the ball radius, $\sigma_c = f(R_b^{-1/3})$, and therefore no longer constant. This statement sparked controversy and a flaw statistics approach[19] was proposed[20] instead of relying on the single maximal stress. Attempts were made to determine the flaw distribution which would correspond to observations, but no satisfactory flaw distribution was found[6] for all indenter sizes, except for a cubic flaw distribution matching a linear dependency well[21] in some cases. Turner et al.[14] formulated the hypothesis that the Hertz theory of contact cannot be used because of large deformations, or because of elastic mismatch between the

specimen and the ball, which was later studied by Johnson et al.,[22] Warren and Hills,[23] Paliwal et al.,[15] and Wereszczak et al.[24] Experiments with uniform damage of surface[25] showed that flaw size has no effect on the fracture load or even that severe abrasion decreases the load. Harrison and Wilks[26] studied the effect of crack size density on the fracture load and claimed that the Auerbach law is applicable if large flaws are rare in comparison to smaller ones, and their density is low.

Roesler[27] pointed out the insufficiency of the flaw statistics approach (similar scatter for small and large indenters) and proposed another approach based on the energy balance,[28] which could be used for determining the specific surface energy associated with crack initiation.[29] Frank and Lawn[30] developed a model which predicted stable growth of a shallow ring crack before fracture. Stable crack could not be observed[25]; thus, this work supported the evidence against the flaw statistics approach but could not validate the energy balance hypothesis. Hamilton and Rawson[8] did not observe any stable crack growth either and did not accept their criticism of flaw statistics despite moderately satisfactory explanation by the flaw statistics. However, Mikosza and Lawn[31] followed a section-and-etch study that observed, contrary to the Hamilton and Rawson,[8] a stable shallow ring crack growth. However, other methods failed to verify it. Later, Dai et al.[32] analyzed the stress intensity factor around the front of semielliptic surface flaws and concluded that such flaw will generally run around to form a ring crack before extending into the depth. This observation has been also demonstrated recently by Schlacher et al.[2] on alumina ceramics.

The approach of describing the fracture by the flaw statistic was revived by Fischer-Cripps and Collins,[33] applying Weibull statistics to predict the fracture force distribution for arbitrary surface conditions. Fisher-Cripps[34] combined Weibull statistics with the energy balance criterion to predict minimal fracture forces, with questionable match to experiments. Wang et al.[35] tested the model from Fisher-Cripps and demonstrated that it may be used as a predictive tool. Weibull theory was extended in the work of Licht et al.[36] to account for strongly inhomogeneous stress field. Lardner et al.[37] studied thick and thin glass plates using the finite element method and developed a crack initiation mechanism map for glass on different substrates. Wang et al.[38] treated the crack as pileups of Somigliana ring dislocation and reduced the problem to solving a system of Cauchy singular integral equations. They deduced that the crack radius shall be determined by the maximum strain energy release rate criterion. The problem was also modeled using XFEM by Marimuthu et al.[39] and in the framework of finite fracture mechanics (FFM) by Hahn and Becker.[40] Variation of the problem with a flat punch was also modeled by Strobl et al. using the FFM[41] and the phase-field model of fracture.[42,43] Andersson analyzed the effect of friction on the stress field and concluded that the coefficient of friction cannot be significantly reduced by the use of lubricants,[44] and the same materials should be pressed together to eliminate friction. Other conclusion was that friction gives only qualitative explanation of the crack radius but not quantitative. Friction was further investigated by Jelagin and Larsson.[45]

Despite several theories and numerous experiments made on different brittle materials, crack initiation in ceramics upon sphere contact loading seems to be affected by distinct factors. In this work, we aim to shed light onto conditions leading to formation of cracks in brittle materials by applying the FFM approach to the problem of the ring crack initiation. A coupled stress–energy criterion is employed to predict the location of the initial ring crack (offset from the contact zone) and to explain how surface residual stresses play a vital role in predicting the crack initiation force in brittle materials. The model assumes (based on empirical evidence) that the initial shape of the observable crack is a ring and no preexisting flaws (cracks) exist.

## 2 | THEORETICAL APPROACH

### 2.1 | The stress–energy criterion

The classical linear elastic fracture mechanics (LEFM) assumes that a crack, present in the material, propagates when the energy release rate, $G$, overcomes the fracture energy of the material, $G_c$. However, LEFM is unable to predict the nucleation of a crack. An alternative approach, the so-called FFM[46] considers the crack formation as a spontaneous (fracture) event, which occurs when both stress and energy conditions along the prospective crack are fulfilled.[47]

The stress–energy criterion employed, also called coupled criterion (CC), requires that (i) that enough energy $\Pi$ is available to create a crack of length $a_0$, and simultaneously (ii) that the stress $\sigma$ perpendicular to the crack faces is larger than the material tensile strength $\sigma_c$ all along the prospective crack path. Both energy and stress criteria are necessary conditions for fracture, but neither one nor the other is sufficient.[48] Therefore, crack initiation will occur when

$$-\frac{\Pi(a_0)-\Pi(0)}{a_0}\overset{\text{def}}{=}G_{\text{inc}}\geq G_c\wedge\sigma(\text{a})\geq\sigma_c\ \text{for}\ 0\leq a\leq a_0 \tag{4}$$

where $G_{inc}$ is defined as the incremental energy release rate, and $a_0$ is the smallest initial crack length that fulfills the CC. This means that although the stress at a

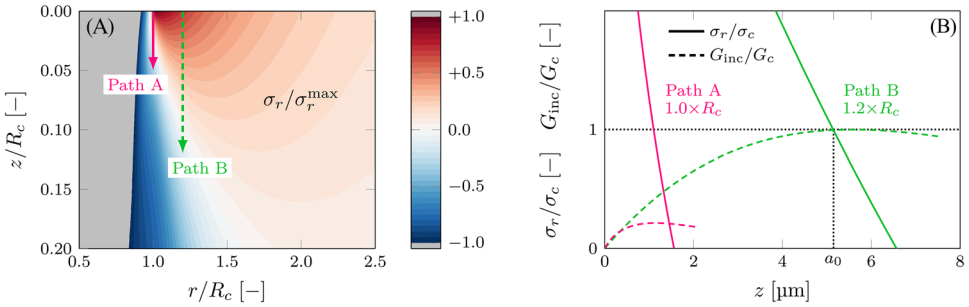


**FIGURE 7** (A) Radial stress field distribution normalized by its maximum at the surface. (B) Example of the coupled criterion evaluation for crack paths at different locations relative to the contact radius for the same applied force.

particular location (e.g., contact radius) may have overcome the material strength, the crack shall not initiate at that location if the energy released by the crack formation is lower than the fracture energy of the material.

Figure 7 illustrates the evaluation of the coupled criterion for crack paths at different locations relative to the contact radius, for the same applied force. Figure 7A depicts the radial stress field[1] normalized by its maximum at the surface in coordinates $r$ and $z$ normalized by the contact radius $R_c$. The (red) region outside the contact radius is under tension, and its magnitude decreases with increasing distance from the contact zone and depth below the surface. Two arrows symbolizing two potential crack paths (one right at the end of the contact zone and the second one with an offset of 20% from the contact radius) are drawn. Two curves for each corresponding path are plotted in Figure 7B: (i) radial stress $\sigma_r$ normalized by the material strength $\sigma_c$ and (ii) the incremental energy release rate $G_{\text{inc}}$ normalized by the fracture energy release rate $G_c$. The fulfillment of the coupled stress–energy criterion can easily be evaluated using this plot for the given loading conditions and position of the crack with respect to the end of the contact zone. The solid line represents the radial stress component as a function of the depth $z$ along the prospective crack path, which decreases from its maximal value on the surface until it becomes smaller than $\sigma_c$ and eventually negative in the compressive region. The magnitude of stress at the surface ($z = 0\ \mu$m) of the path A is bigger than that of the path B, but the stress decreases much rapidly. The dashed line represents the incremental energy release rate corresponding to potential crack depths. This incremental energy release rate starts at 0 J/m$^2$ (the state without a crack) and increases until it reaches $G_c$, where the energy criterion is first satisfied. The ring crack shall then initiate upon that load and/or crack position when both the stress and energy conditions are fulfilled simultaneously, that is, there exist at least one crack depth $a_0$ for which $\sigma/\sigma_c = 1$ and $G_{\text{inc}}/G_c = 1$. The parameter $a_0$ denotes the initial crack length (i.e., ring crack depth). The crack jump from zero length to $a_0$ shall occur upon reaching the crack initiation force $F_c$. As can be inferred from Figure 7B, conditions for (ring) crack initiation are first fulfilled at a certain distance from the contact radius—typically at 1.1–1.2 $R_c$.

The definition of the intrinsic tensile strength, $\sigma_c$, is still a matter of debate. Leguillon et al.[49] defined it as the tensile strength of the material without presence of flaws larger than the average grain size. It should not be confused with the characteristic strength of the material, also called the Weibull strength, associated with the propagation of (pre-existing) flaws that arise upon processing (e.g., pores or inclusions) or machining (e.g., notches or scratches). In an attempt to correlate the microstructural features (e.g., grain size and natural defects) with the material strength, we opt to evaluate the coupled criterion taking $\sigma_c$ as the 1st, 50th, and 99th percentiles of the Weibull strength distribution obtained, for instance, from biaxial bending or uniaxial bending experiments.

## 2.2 | Evaluation of the coupled criterion for various loads and locations

The coupled criterion can be evaluated for many combinations of ball radii, crack radii, and applied forces. For every applied force $F$, the contact radius $R_c$ is calculated by Equation (1), and the contact pressure is prescribed as the boundary condition at the contact surface to the finite element model. The crack initiation force, $F_c$, was sought for every combination of ball radius and crack radius as the minimal applied force that fulfills the stress–energy coupled criterion. Figure 8 depicts the results of evaluating (i) only the stress criterion and (ii) the coupled criterion for a given ball size and a combination of different crack radii and applied forces. Both stress and energy criteria are fulfilled in the corresponding upper (green) region and unfulfilled in the lower (brown) region. The interface

[1] Figure 7A is generated using analytical equation of Huber [4] and the LaTeX package PGFPLOTS.

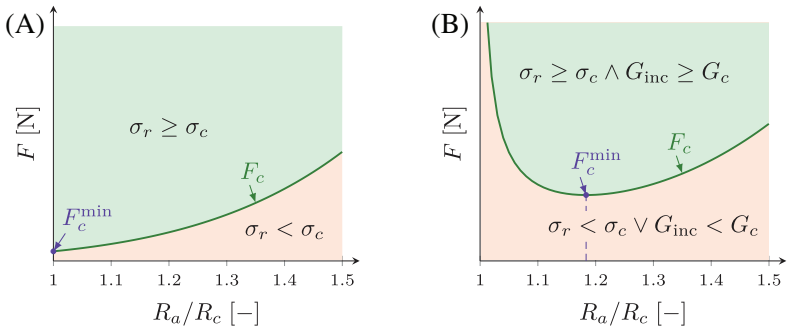


**FIGURE 8** Result of evaluating (A) the stress criterion only and (B) the coupled criterion.

between the two regions (green curve) designates the lowest fracture force $F_c$ necessary to initiate a crack with a given crack radius $R_a$ normalised by the contact radius $R_c$. This curve sets a minimum value for the fracture force, $F_c^{\min}$, which is the minimal force required to initiate a crack: in Figure 8A is given according to the stress criterion and in Figure 8B according to the coupled criterion, respectively.

Figure 8A depicts fulfillment of the stress criterion. The maximum of the radial stress is located at the contact radius as given by Equation (3), and it decreases with $r^{-2}$. Therefore, it should be more convenient for a crack to initiate at the contact radius rather than outside—which is contradicted by empirical data. Moreover, the fracture force would be much lower than that experimentally observed. On the other hand, Figure 8B depicts the fulfillment of the coupled criterion. In the upper (green) region, the stress is greater than the strength, and the energy release rate is greater than the fracture energy. In the lower (brown) region, the stress or the energy (or both) are smaller than their respective critical values. An important result from the calculations is that the $F_c^{min}$ from the CC is typically located outside the contact radius (see Figure 8B). Although the maximum radial stress is at the contact radius, it decreases rapidly into the compression zone. As a consequence, the energy criterion may not be fulfilled at $R_c$. The prediction of the crack location using CC is in a good agreement with the empirical data, and it can explain the event of the crack formation without assuming a presence of small defects or any particular distribution of them.

## 2.3 | Evaluation of stress and incremental energy release rate

To calculate the stress and the incremental energy release rate for different combinations of loading (i.e., applied forces), geometry (i.e., ball radii and crack locations), and materials combinations, an axisymmetric finite element model was developed using the commercial finite element software Ansys Mechanical. Since solving the nonlinear contact problem for many combinations of forces and crack sizes is very demanding, the problem was simplified by replacing the contact problem with the corresponding contact pressure

$$p\ (r) = \sqrt[3]{\frac{6E_c^2 F}{\pi^3 R_b^2}}\ \sqrt[2]{1 - \frac{r^2}{R_c^2}} \tag{5}$$

calculated using the Hertz theory. The accuracy of this simplification was verified by its comparison with a contact simulation on one specific case.

The meridian plane section was discretized by a finite element mesh. The mesh consists of 2D 8-node quadratic structural elements PLANE183 with the axisymmetric option. The edge length of elements in the region of contact was 1 $\mu$m, and along the path of the presumed crack 0.1 $\mu$m or smaller. The element size then increases with a distance from the contact region. The radial displacement was fixed at the symmetry axis, and the axial displacement was fixed at the bottom of the model with a prescribed boundary condition $u_z = 0$. The residual stress profile was incorporated into the model in a form similar to that of the experiments of Angerer and Strobl[17]:

$$\sigma_{\text{res},r}\ (z) = \sigma_{\text{res},\theta}\ (z) = \sigma_{\text{res}}^{\max}\ \cdot e^{-d\cdot z} \tag{6}$$

where $\sigma_{\text{res},r}$ and $\sigma_{\text{res},\theta}$ are radial and tangential components of the residual stress, respectively. The term $\sigma_{\text{res}}^{\max}$ is the compressive residual stress at the surface, which decreases with an increasing depth according to the parameter $d$.

Figure 9 depicts an exemplary evaluation of the CC for an applied force that is twice smaller than the experimentally observed forces. The CC is fulfilled in Figure 9A at ~5 $\mu$m. A typical initial ring crack depth predicted by the coupled criterion is between 2 and 10 $\mu$m. The incorporation of a residual stress gradient, as depicted in Figure 9B, influences not only the resulting stress field, but it has also an impact on the incremental energy release rate, as depicted in Figure 9C.

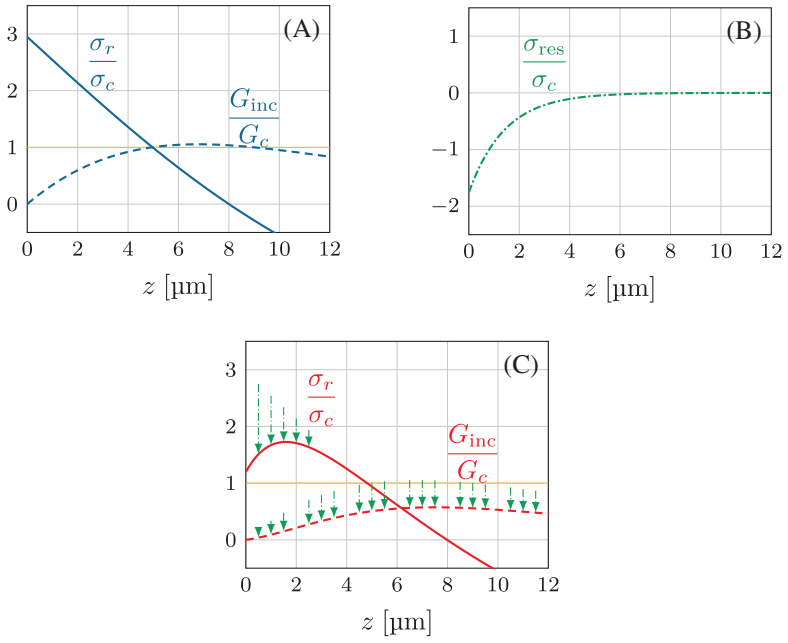


**FIGURE 9** Demonstration of evaluation of the coupled criterion (A), (C) for the same applied load. When the residual stress profile (B) is ignored (A), the CC is fulfilled but when considered (C), the CC is not fulfilled.

For a single ball size, several combinations of $\sigma_{\text{res}}^{\max}$ and $d$ values may result in a match with experiments. However, when multiple ball sizes are considered, there will be only a single value of $\sigma_{\text{res}}^{\max}$ and $d$ resulting in a match across all ball sizes. Hence, when experiments are conducted with different balls, the unique stress profile inside the specimen can be identified.

## 3 | COMPARISON OF SIMULATION RESULTS WITH EMPIRICAL OBSERVATIONS

In this section, we compare different experiments available in the literature and some unpublished experiments with our model to assess the crack initiation upon ball indentation. Models with or without induced surface residual stresses are compared.

### 3.1 | SiC indented by SiC balls

The experiment of Wade et al.[13] used an SiC ball with Young's modulus $E_b = 400$ GPa and Poisson's ratio $\nu_b = 0.18$. Material properties of the SiC specimen (variant U) were as follows: Young's modulus $E_s = 400 \pm 1$ GPa, Poisson's ratio $\nu_s = 0.18$, and fracture toughness $K_{\text{Ic}} = 2.94$ MPa m$^{1/2}$. The characteristic strength was $\sigma_0 = 626$ MPa and the Weibull modulus $m = 8$ determined by the B3B test on the sample F in Ref. [50]. Since crack sizes were not published for individual cracks, we assign them $R_a/R_c = 1.15$ which was calculated from table 3 in Ref. [13]. We understand from the paper that the specimen was annealed at 2000°C for a selected dwell time. The time was chosen such that the microstructure remains unimodal or homogeneous (i.e., there is no abnormal grain growth or elongation), but residual stresses are relaxed. Figure 10 exhibits a good agreement between model predictions and experiments,[13] and in this case, the presence of residual stresses can be ignored.

### 3.2 | $Si_3N_4$ indented by $Si_3N_4$ balls

The work of Rohr[12] (methodology described in Ref. [2]) revealed the strong impact of annealing on the crack initiation force (Figure 5). The experiment used an $Si_3N_4$ ball with Young's modulus $E_b = 307$ GPa and Poisson's ratio $\nu_b = 0.27$. Material properties of the $Si_3N_4$ specimen were as follows: Young's modulus $E_s = 297$ GPa, Poisson's ratio $\nu_s = 0.27$, and fracture toughness $K_{\text{Ic}} = 4.3$ MPa m$^{1/2}$. The characteristic strengths and Weibull moduli were $\sigma_0 = 1048$ MPa and $m = 5.5$ for non-annealed and $\sigma_0 = 1465$ MPa and $m = 15$ for annealed specimens, respectively, measured under biaxial bending using the Ball-on-three-Balls (B3B) test on the sample G in Ref. [51]. Figure 11 shows a comparison of the model predictions with experiments for (i) non-annealed and (ii) annealed specimens, respectively. In the non-annealed case, fracture forces appear to be bound by curves corresponding to a CC evaluation using the lower and upper values of the characteristic strength (Figure 11A). In the annealed case, the characteristic strength increases significantly, most likely associated with the glassy phase filling the defects.[51] Nevertheless, forces required to induce a ring crack drop beyond CC predictions (Figure 11B). A possible explanation

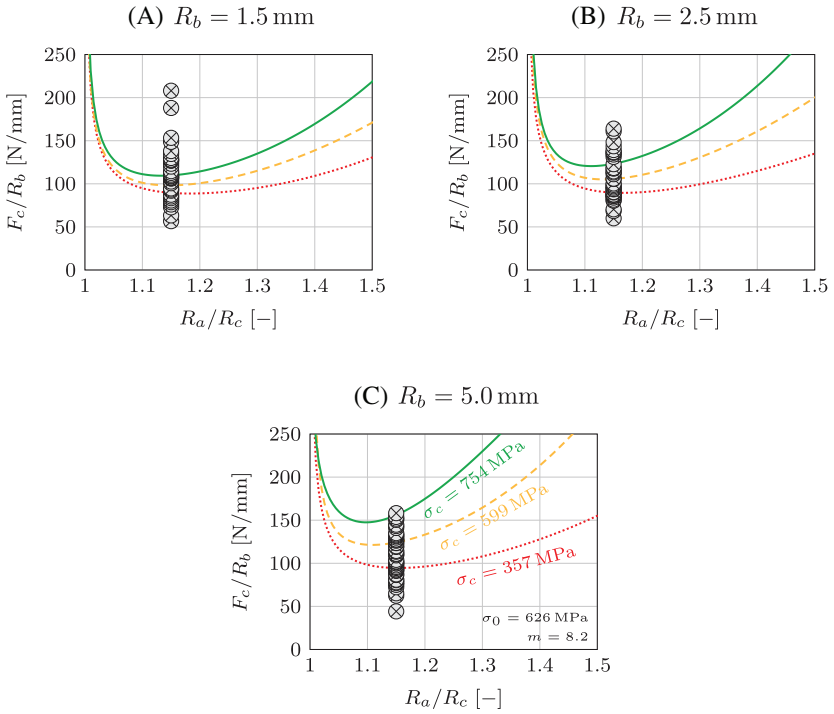


**FIGURE 10** Predictions from the simulation of the silicon carbide indented by silicon carbide ball compared with corresponding experiments. *Source*: The experimental values are adopted from Ref. [13].

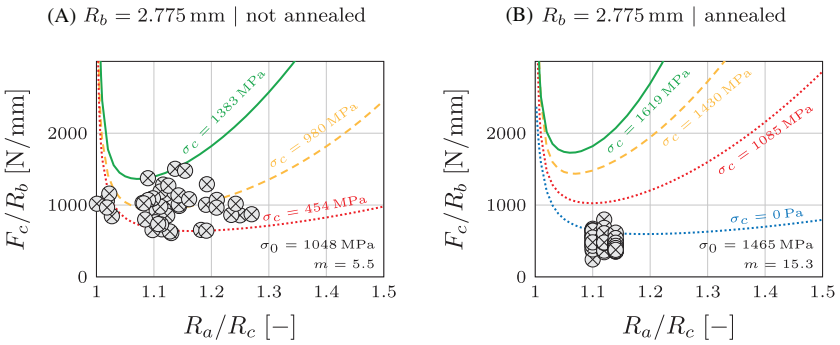


**FIGURE 11** Predictions from the simulation of the silicon nitride indented by silicon nitride balls without induced residual stresses compared with experiments[12] (methodology described in Ref. [2]) (A) without and (B) with annealing in vacuum at 1340°C for 5 h.

may be a change in the material properties due to the annealing process. However, this has not been validated experimentally and is out of the scope of this work.

## 3.3 | SiC indented by diamond balls

In these experiments, a diamond ball with Young's modulus $E_b = 1141$ GPa and Poisson's ratio $\nu_b = 0.07$ was used.[11] Material properties of the silicon carbide (grade HPN) specimen taken for the model were as follows: Young's modulus $E_s = 446 \pm 1$ GPa, Poisson's ratio $\nu_s = 0.154 \pm 0.003$, and fracture toughness $K_{Ic} = 4.13 \pm 0.07$ MPa m$^{1/2}$. The characteristic strength was $\sigma_0 = 626$MPa and the Weibull modulus $m = 8$ determined by the B3B test on the sample F in Ref. [50]. Figure 12 depicts prediction from simulation for three different ball sizes without (a–c) and with (e–g) best fitting residual stress profile $-1.3\ \mathrm{GPa} \times \exp(-0.7\ z)$. Although no information about a scatter of the crack size was published, it was mentioned[11] that they were predominantly between 1.1 and 1.2 multiple of the contact radius. The coupled criterion with the assumed residual stress gives the magnitude and the location of cracks, whereas CC without residual stresses underestimates crack initiation forces.

## 3.4 | $Al_2O_3$ indented by WC balls

In experiments by Schlacher et al.,[2] tungsten carbide balls with Young's modulus $E_b = 650$ GPa and Poisson's ratio $\nu_b = 0.21$ were employed. The material properties of $Al_2O_3$ material specimens were as follows: Young's modulus $E_s = 380 \pm 12$ GPa,[52] Poisson's ratio $\nu_s = 0.22$,[53] and fracture toughness $K_{Ic} = 3.9 \pm 0.4$ MPa m$^{1/2}$.[52] The characteristic strength was $\sigma_0 = 437$ MPa and

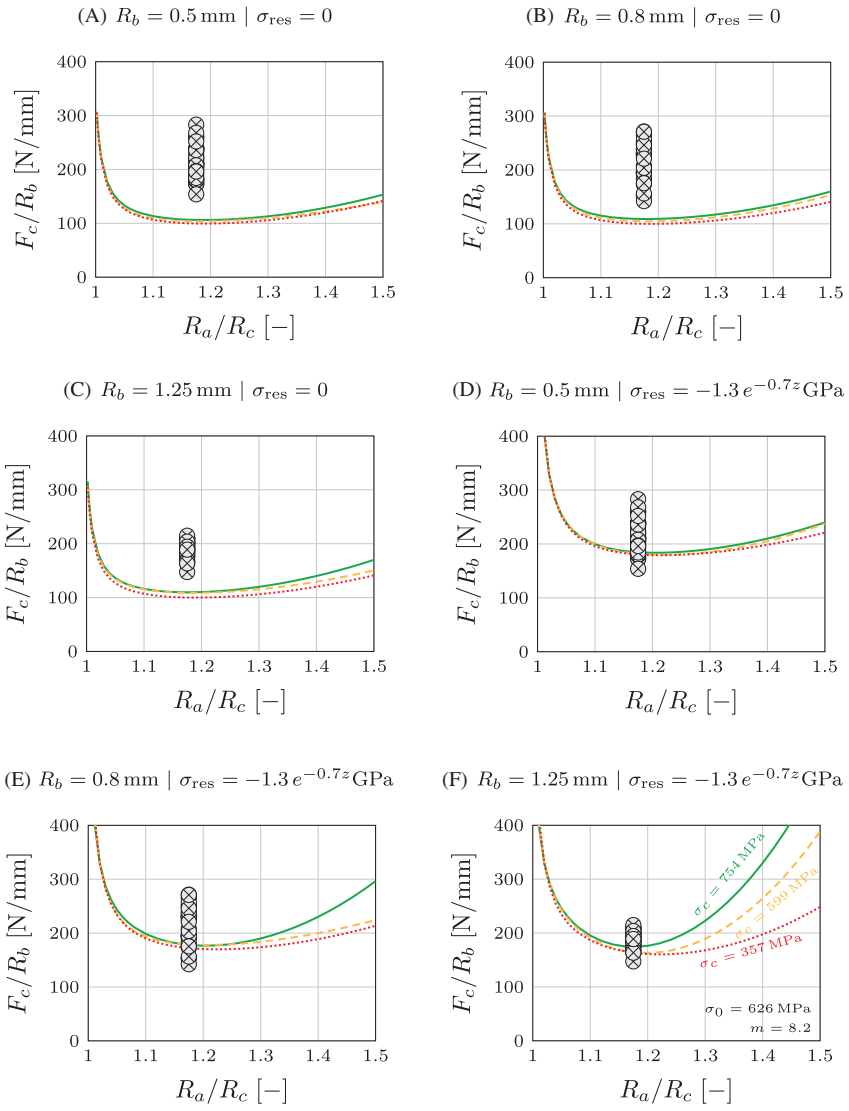


**FIGURE 12** Predictions from simulation of silicon carbide indented by diamond balls with different residual stresses compared with experiments.[11]

the Weibull modulus $m = 10$ determined by the 4-point-bending test.[52] Figure 13 depicts prediction from simulation for three different ball sizes without (a–c) and with (e–g) best fitting residual stress profile $-1.2\,\text{GPa} \times \exp(-0.7\,z)$. The typical shift of relative crack size does not occur with large balls in experiment but is still predicted by the simulation. Residual stress helps with obtaining the fit with magnitude of forces, but the crack size is predicted smaller by the CC.

## 3.5 | $Si_3N_4$ indented by WC balls

The same tungsten carbide (WC) balls as in Section 3.4 were pressed onto a silicon nitride ($Si_3N_4$) (methodology described in Ref. [2]) with following material properties[16]: Young's modulus $E_s = 305 \pm 5$ GPa, Poisson's ratio $\nu_s = 0.25 \pm 0.1$, fracture toughness $K_{\text{Ic}} = 4.3 \pm 0.2\,\text{MPa m}^{1/2}$. The characteristic strength was $\sigma_0 = 1048$ MPa and the Weibull modulus $m = 5.5$ determined by the B3B test on the sample G in Ref. 51. Figure 14 depicts prediction from simulation for two different ball sizes. Residual stress profile was assumed as $-1.2\,\text{GPa} \times \exp(-1.1\,z)$, which corresponds to an XRD measurement.[17] Although the fracture forces magnitude matches experiments well, the relative crack size does not.

## 3.6 | Glass indented by steel balls

Experiments of Mouginot and Maugis[9] used a steel ball with Young's modulus $E_b = 210$ GPa and Poisson's ratio $\nu_b = 0.33$. Material properties of the borosilicate glass specimen were as follows: Young's modulus $E_s = 80$ GPa, Poisson's ratio $\nu_s = 0.22$, the fracture toughness $K_{\text{Ic}} = 0.9\,\text{MPa m}^{1/2}$ and the strength was approximately $\sigma_c = 90$ MPa. Their work contains two sets of surface

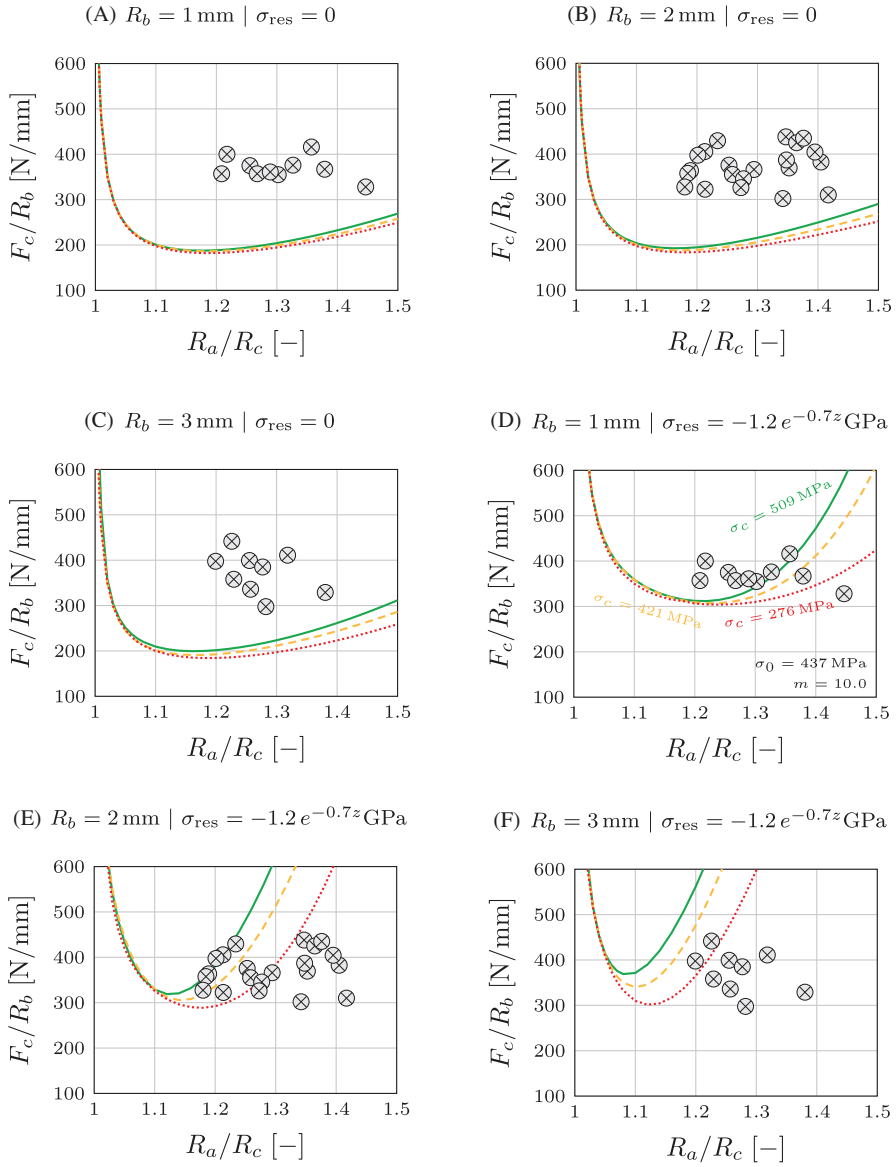


**FIGURE 13** Predictions from the simulation of an alumina indented by WC balls with different surface residual stresses compared with experiments.[2]

machining—one, which is abraded by an SiC paper, and the other, polished by a diamond paste. Figure 15 shows a good match of simulations without residual stress with the set of SiC paper abraded specimens. As the abrasion matches well with simulations, we argue that the abrasion causes grains of material to be ripped of the surface and no residual stresses are introduced. To obtain match also with the polished set, parameters of the model need to be modified. Hahn and Becker[40] proposed adjusting the strength of glass from the common 90 MPa to approximately 790 MPa and the fracture toughness from the common 0.7 MPa $m^{1/2}$ to approximately 1.44 MPa $m^{1/2}$. Although this would result in a match, we consider such high strength and fracture toughness rather overestimated for glass. Instead, we obtain an accurate fit with the set of polished specimens by incorporating the residual stress profile in the form $-400\,\text{MPa} \times \exp(-0.4\,z)$.

## 4 | SUMMARY AND CONCLUSIONS

A stress–energy criterion was introduced to explain the onset and location of ring cracks upon contact loading in brittle materials. A ring crack shall initiate if two conditions are fulfilled simultaneously: (i) the stress along the prospective crack path is larger than the inherent strength of the material, and (ii) the incremental energy upon crack propagation exceeds the fracture energy of the material. Near the contact zone the stresses are relatively high, being up to nine times the tensile strength of the material.

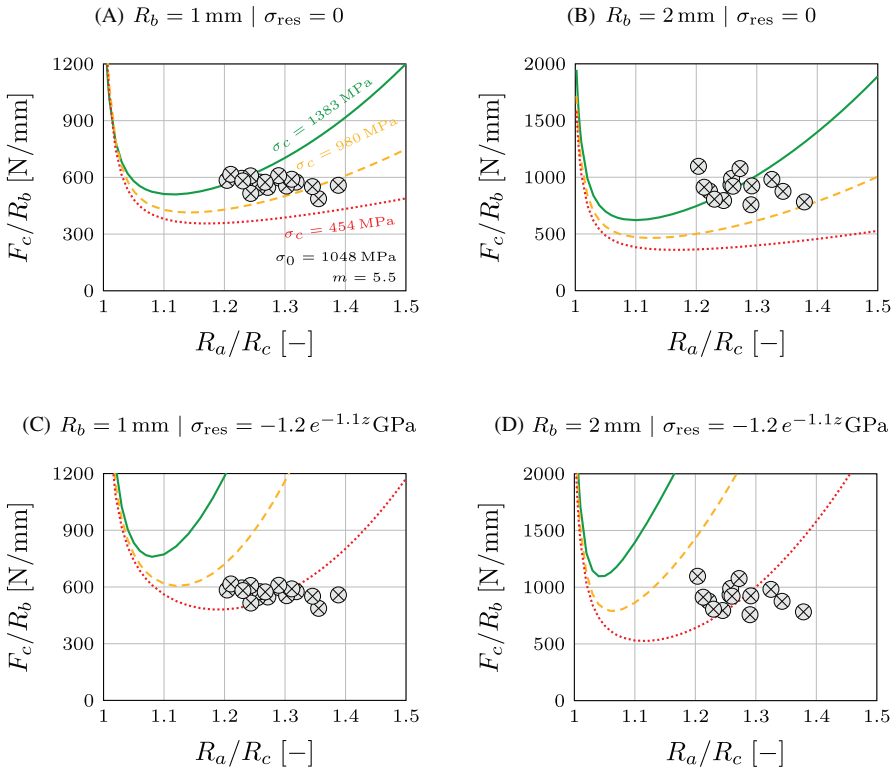


**FIGURE 14** Predictions from the simulation of the silicon nitride indented by WC balls with different surface residual stresses compared with experiments[16] (methodology described in Ref. [2]).

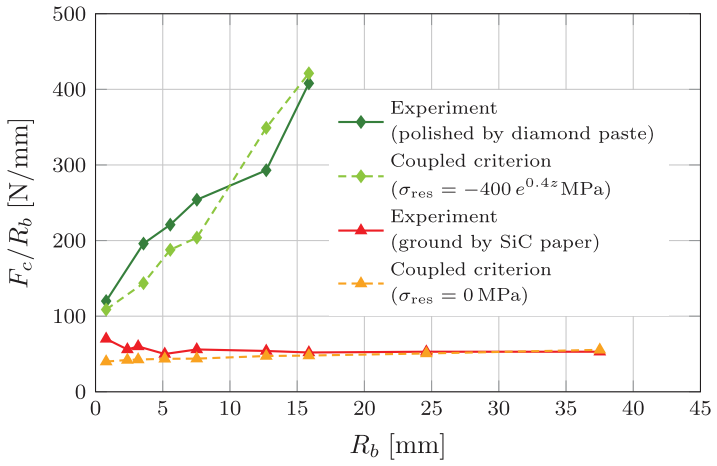


**FIGURE 15** Predictions from the simulation of a glass with and without residual stress indented by steel balls compared with experiments[9] with polished and ground surfaces.

However, the energy condition may not be fulfilled. It means that fracture very close to the contact radius is possible but highly unlikely because the forces required are much higher than at the "critical" distance from the contact radius. At certain distance from the contact area, the incremental energy increases and eventually fulfill the energy condition, leading to the initiation of the ring crack with an offset between 10% and 40% with respect to the contact zone radius. Thus, the Auerbach law is a natural consequence of fulfilling the stress–energy criterion. In this regard, different regimes for the dependence of fracture forces on the ball radius was explained by the coupled criterion, that is, the stress and energy criterion not being fulfilled at the same time. The location of crack relative to the contact radius is also explained by the coupled criterion, as the fracture force required to initiate the crack at the contact radius would be significantly higher than at a location further outside of the contact area.

The force necessary for ring crack initiation can be predicted if the surface condition is taken into account. For instance, compressive residual stresses at the surface must be considered in the model to reproduce the

experimental observations. Consequently, the stress–energy criterion may also be used for estimating residual stresses induced by grinding or polishing by comparing predictions of crack initiation for contact situations with two different ball sizes. Residual stress distributions may be introduced in the models until the best fit to the crack initiation forces is found. The applicability of this criterion can be extended to other types of brittle materials.

## ACKNOWLEDGMENTS

Research was funded by the European Research Council (ERC) through the Consolidator Grant (program Horizon 2020) for the project "Tailoring Microstructure and Architecture to Build Ceramic Components with Unprecedented Damage Tolerance" (project CeraText 817615). The authors would like to express their gratitude to Josef Schlacher, Abdullah Jabr, Jürgen Rohr, and Peter Supancic for providing experimental data and to Peter Supancic, Tanja Lube, and Dominique Leguillon for fruitful discussions.

## ORCID

*Roman Papšík* https://orcid.org/0000-0001-7182-1293
*Oldřich Ševeček* https://orcid.org/0000-0003-3442-2650
*Éric Martin* https://orcid.org/0000-0003-0688-1649
*Raúl Bermejo* https://orcid.org/0000-0002-6891-3653

## REFERENCES

1. Auerbach F. Absolute härtemessung. Annalen der Physik und Chemie. 1891;279:61–100.
2. Schlacher J, Jabr A, Hofer A-K, Bermejo R. Contact damage tolerance of alumina-based layered ceramics with tailored microstructures. J Am Ceram Soc. 2022;105:1–13.
3. Hertz H. On the contact of elastic solids. J Reine Angew Math. 1881;92:156–71.
4. Huber MT. Zur Theorie der Berührung fester elastischer Körper. Ann Phys. 1904;319:153–63.
5. Tillett JPA. Fracture of Glass by Spherical Indenters. Proc Phys Soc London, Sect B. 1956;69:47–54.
6. Tsai YM, Kolsky H. A theoretical and experimental investigation of the flaw distribution on glass surfaces. J Mech Phys Solids. 1967;15:29–46,
7. Nadeau JS. Hertzian fracture of vitreous carbon. J Am Ceram Soc. 1973;56:467–72.
8. Hamilton B, Rawson H. The determination of the flaw distributions on various glass surfaces from Hertz fracture experiments. J Mech Phys Solids. 1970;18:127–47.
9. Mouginot R, Maugis D. Fracture indentation beneath flat and spherical punches. J Mater Sci. 1985;20:4354–76.
10. Miller PD, Bowman KJ. Hertzian fracture of textured $Si_3N_4$. Acta Mater. 1996;44:3025–3034.
11. Wereszczak AA, Johanns KE, Jadaan OM. Hertzian ring crack initiation in hot-pressed silicon carbides. J Am Ceram Soc. 2009;92:1788–95.
12. Rohr J. Akustische Detektion von Erstschädigung in Siliziumnitrid. Leoben: Montanuniversität Leoben. 2012.
13. Wade J, Ghosh S, Claydon P, Wu H. Contact damage of silicon carbide ceramics with different grain structures measured by Hertzian and Vickers indentation. J Eur Ceram Soc. 2015;35:1725–36.
14. Turner DN, Smith PD, Rotsey WB. Hertzian stress cracks in Beryllia and glass. J Am Ceram Soc. 1967;50:594–8.
15. Paliwal B, Tandon R, Buchheit TE, Rodelas JM. An assessment of the effectiveness of the Hertzian indentation technique for determining the fracture toughness of brittle materials. J Am Ceram Soc. 2011;94:2153–61.
16. Jabr A. Contact damage of alumina-based layered ceramics with tailored microstructure. Leoben: Montanuniversität Leoben, 2022.
17. Angerer P, Strobl S. Equi-penetration grazing incidence X-ray diffraction method. Acta Mater. 2014;77:370–8.
18. Lawn BR. Indentation of ceramics with spheres: a century after Hertz. J Am Ceram Soc. 1998;81:1977–94.
19. Weibull W. A statistical distribution function of wide applicability. ASME J Appl Mech. 1951;18:293–7.
20. Gibbs P, Cutler IB. On the fracture of glass which is subjected to slowly increasing stress. J Am Ceram Soc. 1951;34:200–6.
21. Fisher GMC. The auerbach range in the Hertzian fracture of glass. J Appl Phys. 1967;38:1781–6.
22. Johnson KL, O'Connor JJ, Woodward AC. The effect of the indenter elasticity on the Hertzian fracture of brittle materials. Proc R Soc A: Math Phys Eng Sci. 1973;334:95–117.
23. Warren PD, Hills DA. The influence of elastic mismatch between indenter and substrate on Hertzian fracture. J Mater Sci. 1994;29(11):2860–6.
24. Wereszczak AA, Daloz WL, Strong KTJ, Jadaan OM. Effect of indenter elastic modulus on Hertzian ring crack initiation in silicon carbide. Int J Appl Ceram Technol. 2011;8:885–94.
25. Langitan FB, Lawn BR. Hertzian fracture experiments on abraded glass surfaces as definitive evidence for an energy balance explanation of Auerbach's law. J Appl Phys. 1969;40:4009–17.
26. Harrison J, Wilks J. The Hertz indentation test and Auerbach's law. J Phys D: Appl Phys. 1978;11:73–81.
27. Roesler FC. Indentation hardness of glass as an energy scaling law. Proc Phys Soc London, Sect B. 1956;69:55–60.
28. Griffith AA. The phenomena of rupture and flow in solids. Philos Trans R Soc. 1920;221:163–98.
29. Roesler FC. Brittle fractures near equilibrium. Proc Phys Soc London, Sect B. 1956;69:981–92.
30. Frank FC, Lawn BR. On the theory of Hertzian fracture. Proc R Soc A. 1967;299:291–306.
31. Mikosza AG, Lawn BR. Section-and-etch study of Hertzian fracture mechanics. J Appl Phys. 1971;42:5540–5.
32. Dai DN, Hills DA, Warren PD, Nowell D. The propulsion of surface flaws by elastic indentation testing. Acta Metall Mater. 1995;43:985–91.
33. Fischer-Cripps AA, Collins RE. The probability of Hertzian fracture. J Mater Sci. 1994;29:2216–30.
34. Fischer-Cripps AC. Predicting Hertzian fracture. J Mater Sci. 1997;32:1277–85.

35. Wang R, Katsube N, Seghi RR, Rokhlin SI. Failure probability of borosilicate glass under Hertz indentation load. J Mater Sci. 2003;38:1589–96.
36. Licht V, Hülsmeier P, Fett T. Probability of cone crack initiation due to spherical contact loading. J Eur Ceram Soc. 2004;24:2907–15.
37. Lardner TJ, Ritter JE, Zhu G-Q. Spherical indentation and fracture of glass plates. J Am Ceram Soc. 1997;80:1851–62.
38. Wang X-Y, Kwok-Yan Li L, Mai Y-W, Shen Y-G. Theoretical analysis of Hertzian contact fracture: ring crack. Eng Fract Mech. 2008;75:4247–56.
39. Marimuthu KP, Rickhey F, Lee JH, Lee H. Spherical indentation for brittle fracture toughness evaluation by considering kinked-cone-crack. J Eur Ceram Soc. 2017;37:381–91.
40. Hahn J, Becker W. Determination of strength and fracture toughness from indentation tests in the framework of finite fracture mechanics. In: Atluri SN and Vušanović I, editors. Computational and experimental simulations in engineering. Springer International Publishing; 2021. p. 44–51
41. Strobl M, Dowgiałło P, Seelig T. Analysis of Hertzian indentation fracture in the framework of finite fracture mechanics. Int J Fract. 2017;206:67–79.
42. Strobl M, Seelig T. Analysis of Hertzian indentation fracture using a phase field approach. In: *Proceedings in Applied Mathematics and Mechanics (PAMM)*, 2019.
43. Strobl M, Seelig T. Phase field modeling of Hertzian indentation fracture. J Mech Phys Solids. 2020;143:1–34.
44. Andersson M. Stress distribution and crack initiation for an elastic contact including friction. Int J Solids Struct. 1996;33:3673–96.
45. Jelagin D, Larsson P-L. On indentation and initiation of fracture in glass. Int J Solids Struct. 2008;45:2993–3008.
46. Hashin Z. Finite thermoelastic fracture criterion with application to laminate cracking analysis. J Mech Phys Solids. 1996;44:1129–45.
47. Weißgraeber P, Leguillon D, Becker W. A review of finite fracture mechanics. Arch Appl Mech. 2016;86:375–401.
48. Leguillon D. Strength or toughness? Eur J Mech A Solids. 2002;21:61–72.
49. Leguillon D, Martin É, Ševeček O, Bermejo R. What is the tensile strength of a ceramic to be used in numerical models for predicting crack initiation? Int J Fract. 2018;212:89–103.
50. Harrer W, Danzer R, Rendtel A. Influence of the surface condition on the biaxial strength of a commercial silicon carbide. J Eur Ceram Soc. 2016;36:3895–900.
51. Harrer W, Danzer R, Morrell R. Influence of surface defects on the biaxial strength of a silicon nitride ceramic—increase of strength by crack healing. J Eur Ceram Soc. 2012;32:27–35.
52. Hofer A-K, Walton R, Ševeček O, Messing GL, Bermejo R. Design of damage tolerant and crack-free layered ceramics with textured microstructure. J Eur Ceram Soc. 2020;40:427–35.
53. Chang Y, Bermejo R, Ševeček O, Messing GL. Design of alumina-zirconia composites with spatially tailored strength and toughness. J Eur Ceram Soc. 2015;35:631–40.

**How to cite this article:** Papšík R, Ševeček O, Martin É, Bermejo R. Prediction of ring crack initiation in ceramics and glasses using a stress–energy fracture criterion. J Am Ceram Soc. 2023;106:4329–4342.
https://doi.org/10.1111/jace.19076